

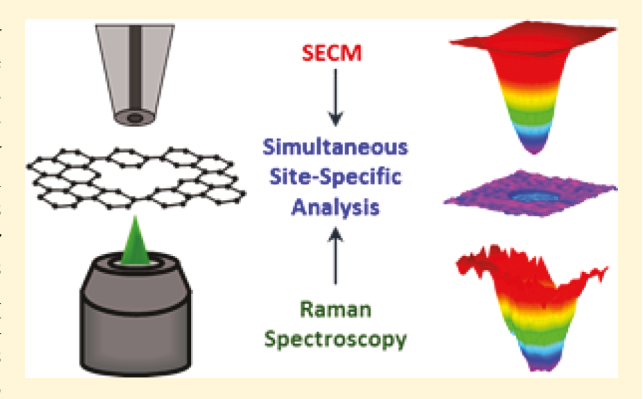
Probing Graphene Interfacial Reactivity via Simultaneous and Colocalized Raman—Scanning Electrochemical Microscopy Imaging and Interrogation

Noah B. Schorr, Annie G. Jiang, and Joaquín Rodríguez-López*

Department of Chemistry, University of Illinois at Urbana-Champaign, 600 South Mathews Avenue, Urbana, Illinois 61801, United States

Supporting Information

ABSTRACT: Addressing challenges in interfacial electrochemistry requires multimodal approaches that correlate the local structure and reactivity of materials with high spatial and temporal versatility. Here, we introduce spatiotemporally correlated Raman spectroscopy and scanning electrochemical microscopy (SECM) to study the impact that structural heterogeneities, interfacial decomposition products, and layer number have on the electron-transfer properties of graphene electrodes. By colocalizing the SECM probe and laser line, we successfully obtained congruent SECM and Raman images at a rate of 5 s per pixel with sub-10 μ m resolution, obtaining full spectra per pixel at a signal-to-noise ratio as high as ~20. SECM imaging of a micropatterned graphene electrode showed its reactivity to be highly dependent on the intensity of the G peak,



an indicator of the number of graphene layers. We further monitored the impact of excursions to positive potentials using the [Fe(CN)₆]^{3-/4-} redox pair as mediator. Raman-SECM allowed us to decouple the contributions to the redox response of different structural effects including exfoliation, increase in defect density, and surface film formation, on the same site and in real time. The coupling of in situ Raman spectroscopy and SECM provides a powerful surface-sensitive analytical approach to elucidate interfacial properties relevant to energy, catalysis, and sensing.

Inderstanding the intertwining roles of structure and reactivity on electrochemical interfaces requires the development of unique multimodal imaging techniques. In situ spectroelectrochemical approaches have been very successful at eliminating the uncertainties associated with analyzing a sample under different environments and experimental conditions. 1-4 An improvement in the diagnostic value of spectroelectrochemical methods is the acquisition of data sets that are additionally matched in temporal and spatial resolution. This would help elucidate quantitative site-specific correlations between reactivity and structure. Here we introduce such an approach, taking advantage of colocalized scanning electrochemical microscopy (SECM) and Raman spectroscopy. The merger of these techniques is advantageous due to the match in interrogation spot size and time scale of data acquisition, thus allowing the real-time observation of changes in structure and reactivity on single sites.

Here, we generate both images and time-dependent data sets of coupled vibrational and redox information gathered in situ. To demonstrate the capabilities of coupled Raman-SECM, we chose to study the electrochemistry of chemical vapor deposition (CVD)-grown multilayer graphene (MLG) samples. The remarkable electronic, optical, and structural properties of single- and multilayer graphene have generated interest in applications reaching from battery and supercapacitors to

nanofiltration and photovoltaics. 5-9 Because of the widespread interest and favorable properties of graphene and its derivatives, such as MLG and graphene oxide, correlating its interfacial properties and reactivity is of high interest. 10

Incorporating Raman spectroscopy to SECM enables the correlation of two techniques strongly suited for MLG. Raman spectroscopy continues to be a standard method for assessing the vibrational and electronic properties of carbon materials from graphite to graphene. The method is especially applicable to in situ investigations because it is nondestructive and is not inhibited by water as a solvent. 16,17 SECM is useful for quantifying kinetic parameters of the interface, solution species, and surface adsorbates, ^{18,19} advantageously decoupling the substrate and tip response. This enables the measurement of real-time changes in the redox reactivity of the substrate. SECM has previously been applied to studying various carbon materials. 18,20-24 While numerous papers have been published on the reactivity of carbon derivatives such as graphene, graphene oxide, and highly ordered pyrolytic graphite (HOPG), there are conflicting accounts as to the correlation between reactivity and structural properties. 10,25-27 The

Received: February 12, 2018 Accepted: April 27, 2018 Published: April 27, 2018

differences in reactivity of the basal and edge planes of graphitic materials have been debated extensively. Likewise, the roles of adsorption and contamination of carbon surfaces have been studied recently. Therefore, knowledge regarding the link between changes in electrode structure and reactivity in situ is highly desirable.

The crucial aspect of coupling Raman spectroscopy and SECM to study surface reactivity is the ability to obtain quantitative information about electron-transfer rates and structure with spatial discrimination. 14,19 Few studies have reported the use of Raman with SECM. 31–33 Our group recently introduced colocalized and temporally correlated Raman—SECM as an effective means to monitor transient processes on monolayer redox-active films. Here, we expand the technique to detect instantaneous changes in redox kinetics as a function of structural surface perturbations. We also produce images of the simultaneously acquired vibrational and electron-transfer reactivity of a surface for the first time. In this work, we explore how the formation of passivating layers and the onset of surface degradation impact the redox properties of the graphene surface.

Controlling the reactivity of electrodes through film formation is central to applications in energy storage, e.g., the solid electrolyte interphase on graphite anodes in lithium ion batteries, ^{34–36} which is of interest to our group. Understanding film formation due to the decomposition of solution-phase redox species is pertinent due to the emergence of redox-flow, mediator-based Li–air and charge-overload protected Li-ion batteries. ^{37–41} The formation of these films results from the degradation of the solution species by processes triggered by the large polarizations applied to battery electrodes. ^{42–44} When combined together to create a platform for an in-depth study of interface characteristics, the methodology presented here provides a multimodal technique applicable to an immense number of materials and future experimental procedures.

■ EXPERIMENTAL SECTION

Chemicals. Ferrocenemethanol (FcMeOH, Sigma-Aldrich, 97%), potassium ferricyanide (K_3 Fe(CN)₆, Sigma-Aldrich, 99+%), and potassium nitrate (KNO₃, Fisher Scientific, 99+%) were purchased from commercial sources and used as received. Millipore deionized water with resistance ≥18 MΩ was used for all solutions. Copper foil, 25 μ m thick, was purchased from Alfa Aesar. Nano 950 K A4 PMMA, and Microposit S1813 photoresist were purchased from MicroChem. AZ 917 MIF developer was purchased from AZ Electronic Materials. CE-100 copper etchant was purchased from Transene Company. Glass coverslips were procured from VWR.

Raman—SECM. We used a modified setup based on the Raman—SECM configuration reported in our previous publication.³² An in-lab constructed inverted microscope was situated to focus a Melles Griot 532 nm laser line to the same region as the SECM probe on a sample surface (Figure 1). A camera (ThorLabs) allowed visualization of the alignment between the focused laser line and the microelectrode. Adjustments to the laser line and microelectrode position were made by maneuvering a micropositioner and piezoelectric mount, respectively. The sample cell was held on a custom-made stage that was manually leveled to ensure proper imaging. A Nikon 40× (N.A. 0.65) objective was used for all measurements. Stokes scattered light was collected in a fiber-optic cable connected to an Ocean Optics QE Pro spectrometer for spectral acquisition. To enable sample imaging

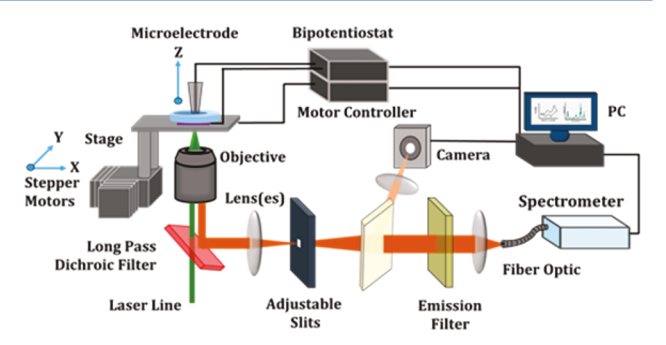


Figure 1. Schematic of the lab-built Raman—SECM setup used for all experiments.

the sample stage was mounted onto an x- and y-stepper motor for sample positioning and imaging. Sample imaging was achieved by moving the stage in the x-direction at a speed of 1 μ m/s while simultaneously taking electrochemical and spectroscopic measurements. The stage was then moved in a 5 μ m y-direction step and continued with rastering in the x-direction until image completion. Spectrum acquisition time was set for 5 s during imaging and 3 s for in situ oxidation experiments.

Growing and Patterning Multilayer Graphene. Multilayer graphene was grown by CVD. Photolithography and reactive ion etching (RIE) were applied to create 50 μ m hole patterns on graphene. A detailed procedure for MLG fabrication and modification can be found in the Supporting Information.

Electrochemical Tests. All electrochemical measurements were performed in a four-electrode cell configuration conducted using a CHI 920D SECM from CH Instruments (Austin, TX). A Ag/AgCl reference was used for all experiments. SECM probes consisted of etched Pt wires sealed in patch clamp glass. For SECM imaging experiments, an SECM probe was fabricated using an etched Pt wire with a diameter of 7 μm and an Rg of 2. For time-dependent measurements, an etched Pt wire with a diameter of 11 μm and Rg = 3 was used. A more detailed procedure for probe fabrication can be found in the Supporting Information. Aqueous solutions of 1 mM FcMeOH with 100 mM KNO₃ and 1 mM [Fe(CN)₆]^{3-/4-} with 100 mM KNO₃ were used for imaging and in situ oxidation experiments, respectively.

■ RESULTS AND DISCUSSION

The Raman spectrum of the untreated MLG shows the characteristic D, G, and 2D peaks of graphene (Figure 2A). The

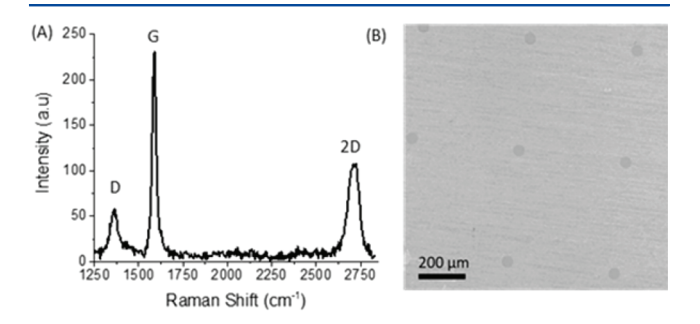


Figure 2. Characterization of graphene. (A) Average Raman spectrum of CVD-grown multilayer graphene. (B) Optical microscope image of the patterned MLG used in Raman—SECM imaging.

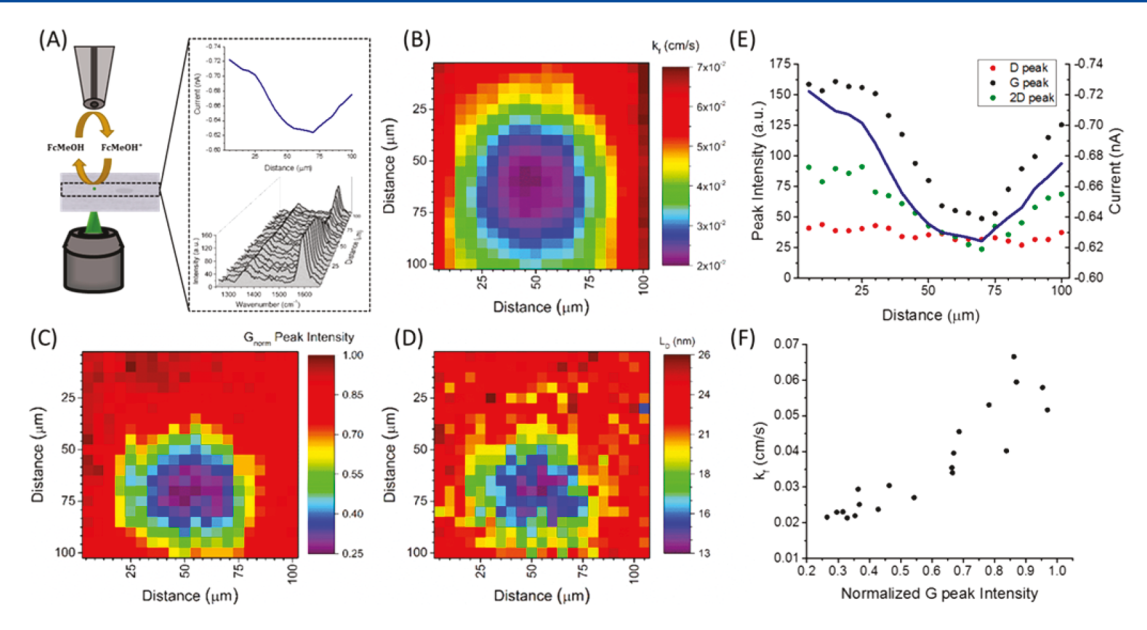


Figure 3. Simultaneous Raman—SECM measurements done with a 3.5 μ m radius Pt ultramicroelectrode (UME) in 1 mM FcMeOH with 100 mM KNO₃ supporting electrolyte. The MLG was held at open-circuit potential for the duration of the experiment. (A) Diagram of experimental alignment between the laser and microelectrode. The small dashed box depicts a single scan in the x-direction to generate electrochemical feedback and spectra, where a row of data was collected in 100 s. (B) Calculated forward electron-transfer rate (k_f) of the graphene surface determined by current feedback at the UME. (C) Image of normalized G peak intensity of the MLG surface. (D) Distance between defects (L_D) determined from I_D/I_G . (E) UME current response and peak intensities of D, G, 2D peaks for one scan in the x-direction over an RIE-modified MLG. (F) Comparison of the k_f and normalized G peak intensity from the same region as panel E.

D peak corresponds to the A_{1g} vibration mode and is activated by disorder in the MLG. 13,45 The G peak arises from an E_{2g} inplane vibration mode that has an increasing intensity with the number of graphene layers. 12,46,47 A ratio of the D peak intensity to the G peak intensity ($I_{\rm D}/I_{\rm G}$) can be used to quantify the distance between defects in graphene, $L_{\rm D}$. A large $I_{\rm D}/I_{\rm G}$ will result in a small $L_{\rm D}$, where a defect is anything that causes the breaking of the sp² carbon bond. 14,24 An example calculation is provided in the Supporting Information (eq S1). The unmodified MLG consists of 10 graphene layers determined from transmittance measurements assuming a loss of 2.3% per graphene layer (Figure S1). 48 An optical image of the patterned MLG can be seen in Figure 2B. Treatment by RIE caused removal of graphene layers in 50 μ m diameter regions across the MLG surface.

Simultaneous Raman–SECM Imaging. We investigated the feedback response and Raman scattering of a patterned MLG electrode. Simultaneous mapping of spectral features and SECM feedback current permitted correlation between changes in reactivity and structure, as shown in Figure 3. Once we aligned the SECM probe and laser line, the stage was rastered to generate position-dependent spectra and electrochemical feedback with comparable 5 s time resolution per pixel and 5 μ m pixel size. Figure 3A depicts the information generated by a single line scan across the MLG surface used to construct the images in Figure 3B–D. Here, the Raman and SECM signal provided high contrast between the region bombarded by RIE and the unperturbed MLG. Mapping of the sample surface confirmed a successful procedure for the alignment of the laser line and SECM probe.

The circular region where layers of graphene were removed produced a lower feedback current than the pristine areas. The feedback current was used to calculate the rate constant (k_f) for electron transfer on the different areas of the sample, Figure 3B, as determined by the theory of Lefrou and Cornut.⁴⁹ These

same regions that exhibited a lower feedback current also showed a lower G peak intensity, Figure 3C. The intensity of the G peak is related to the number of layers of graphene present. Since the pristine MLG consisted of ~ 10 layers, the lowest intensities observed for the G peak at the center of the image corresponded to ~ 3 layers of graphene. In the etched region, the peaks did not shift in wavenumber indicating that the RIE did not cause doping in the sample. The RIE-exposed MLG also has the smallest distance between defects in the sample (Figure 3D). From the simultaneously taken images it is clear that removal of graphene layers changed both the reactivity and structure of the MLG.

Increasing the number of layers of graphene increases the density of states of the surface. ^{25,50} This would account for the higher activity present in the unmodified regions. Substrate effects on the electronic structure are also reduced when more than one layer of graphene is present. ^{51,52} These measurements are in good agreement with previous bulk and spatially resolved measurements of the reactivity differences of graphene layers.^{25,53} To further examine the effect of the number of layers on the $k_{\rm f}$, we analyzed a single scan across the center of the induced defect (Figure 3E). The G peak intensity decreased within the etched region in the same manner as the decrease in current recorded by the microelectrode. Surprisingly, the D peak intensity did not vary across the modified region. Lack of increase in the D peak required the RIE to have removed layers of graphene without introducing a higher concentration of defects in the graphene layers left in the region. The small calculated $L_{\rm D}$ over the etched region is therefore predominantly caused by the decreasing G peak intensity. When the $k_{\rm f}$ is plotted against the G peak intensity for this region a nonlinear trend emerges, demonstrating that the number of layers greatly impacts electron transfer (Figure 3F).

Time-Dependent Raman—SECM Analysis. Alignment of the SECM probe and laser line enables time-resolved analysis of

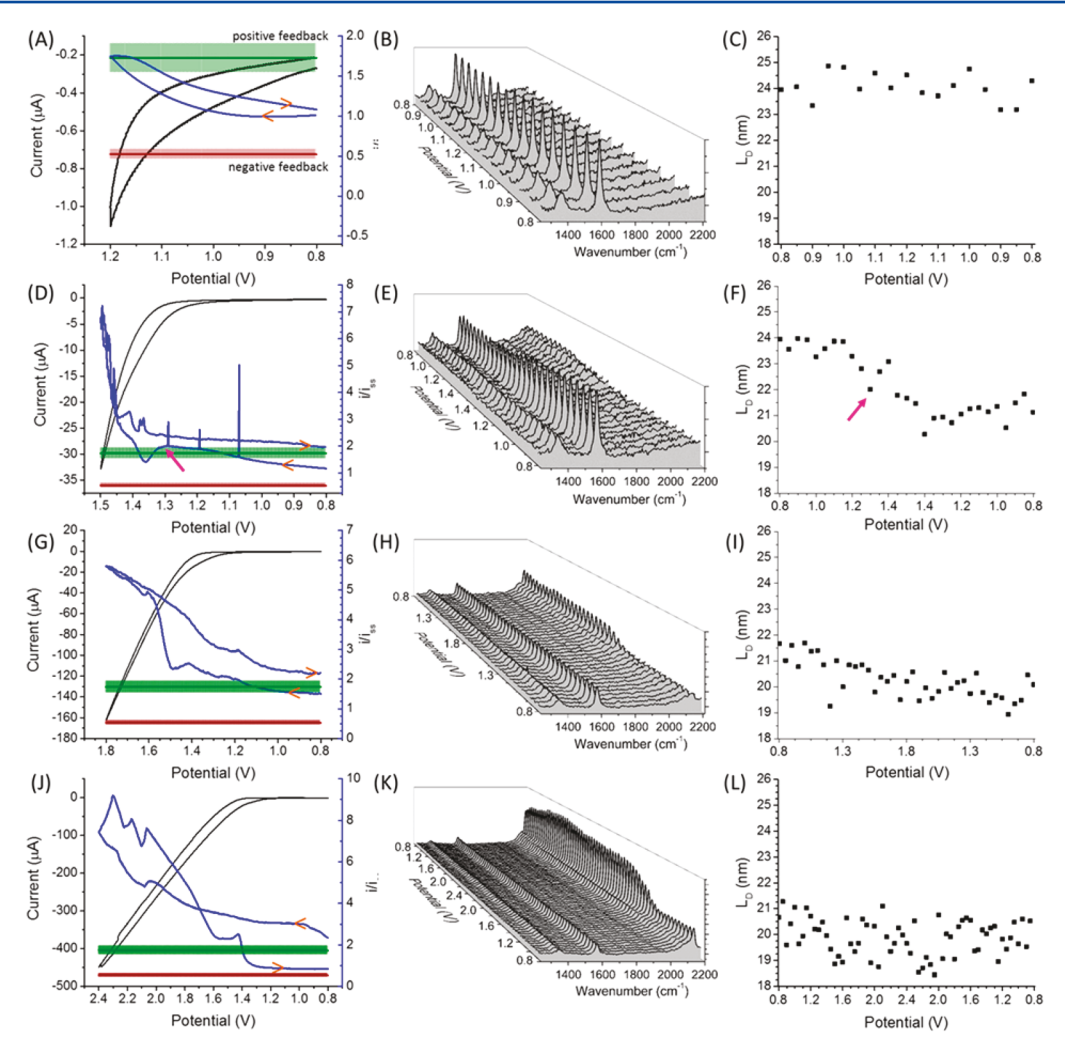


Figure 4. CVs, Raman spectra, and calculated $L_{\rm D}$ values for MLG. Substrate CVs were performed at 10 mV/s, while the tip was held at constant potential for $[{\rm Fe(CN)_6}]^{3-}$ reduction. Orange arrows indicate directionality of the CV scan. Green and red lines in CV plots represent theoretical maximum positive and minimum negative feedback for the SECM probe with 10% error on the feedback current. Tip current, right axis, is normalized by steady-state current spectra taken with 5 s integration time. (A) CV between 0.8 and 1.2 V. (B) Raman spectra taken during the CV in panel A. (C) $L_{\rm D}$ calculated from $I_{\rm D}/I_{\rm G}$. (D) CV between 0.8 and 1.5 V. (E) Raman spectra taken during the CV in panel D. (F) $L_{\rm D}$ calculated from $I_{\rm D}/I_{\rm G}$. (J) CV between 0.8 and 2.4 V. (K) Raman spectra taken during the CV in panel J. (L) $L_{\rm D}$ calculated from $I_{\rm D}/I_{\rm G}$.

spectroscopic and redox information on a single reacting site. To demonstrate the in situ ability to monitor reactivity changes using Raman–SECM, we now turn to the modification of ~10 layer graphene samples by electrochemical oxidation. $^{54-56}$ Expediting oxidation provides a means to study the stability of layered graphene in conditions hostile to the sample integrity. To monitor the modification of MLG, we used the reduction of $[{\rm Fe}({\rm CN})_6]^{3-}$ for evaluating changes in SECM feedback. The slow kinetics of the $[{\rm Fe}({\rm CN})_6]^{3-/4-}$ redox pair have been used previously to amplify the resulting effects changes have on the reactivity of graphene compared to a fast outer-sphere redox mediator. 20,57,58 Likewise, reports on the formation of passivating layers from this species make it a suitable probe for exploring surface modification of MLG. 59,60

To gauge the effect of potential on the MLG, a series of expanding window cyclic voltammograms were performed while simultaneously collecting feedback with the SECM probe and acquiring Raman spectra on the same spot (Figure 4). When the potential was swept in the regime between 0.8 and 1.2 V, both the substrate and tip experienced a larger current with

increasing potential. Near 1.2 V the mass-transfer-limited positive feedback current was reached, as observed by the plateau in Figure 4A. During this sweep there were negligible changes to the Raman spectra and $L_{\rm D}$ of the MLG. This suggests that activation of the redox kinetics in this potential region responds to an increase in overpotential, as predicted by electron-transfer models, and not to structural changes on the MLG. As the potential was scanned to more positive values, marked structural and reactive changes were observed. The progression of the tip current surpassing the theoretical positive feedback level indicates additional processes occurring at the substrate which create additional species detected at the tip, e.g., O_2 from water oxidation.

Two changes to the MLG occur during excursions to more positive potentials as noticeable by the Raman spectroscopy. First, as seen in Figure 4F, the $L_{\rm D}$ decreased concurrently to a dip in the SECM feedback current at 1.36 V (signaled by the arrow in Figure 4, parts D and F). The decrease in $L_{\rm D}$ was caused primarily by a decrease in the G peak intensity and was perpetuated in the following CVs. Such decrease in the G peak

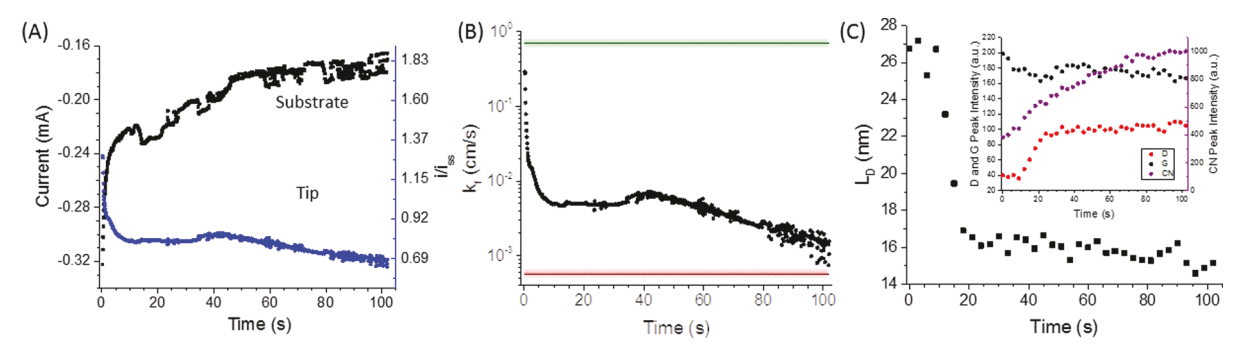


Figure 5. Raman—SECM measurements during MLG oxidation in 1 mM Fe(CN) $_6^{3-/4-}$ with 100 mM KNO $_3$. (A) Current response of the MLG substrate, black, and the UME, blue, to applied 2.5 V for MLG oxidation and 0.05 V to the UME for $[Fe(CN)_6]^{3-/4-}$ reduction. Tip current, right axis, is normalized by steady-state current. (B) Forward rate kinetics (k_i) of MLG during oxidation. Green and red lines in CV plots represent theoretical maximum positive and minimum negative feedback for the SECM probe assuming a tolerance of 5% deviation from the theoretical mass-transfer-limited curve. (C) L_D calculated from the I_D/I_G in panel C. The inset shows the intensity of the D, G, and major C \equiv N peaks.

intensity likely arose from exfoliation of the MLG, and not from the creation of chemical defects (i.e., increasing D peak) which have been reported as increasing electron-transfer rates.^{20,61} A lowered reactivity by exfoliation is also in agreement with the RIE-modified MLG shown in Figure 3. Second, following the dip, new peaks in the Raman spectrum appeared at 2098 and 2160 cm⁻¹ corresponding to a C \equiv N stretch of the $[Fe(CN)_6]^{3-/4-}$ couple (Figure 4E).^{60,62} A change in the MLG interface likely facilitates the surface modification. Inspection of the postmortem MLG samples indeed shows the formation of surface film (Figure S2). Continuing into the CV in Figure 4G, the C≡N peak enlarges by ~300%, leveling in intensity when the potential hits a maximum for the sweep (Figure 4K), but then increasing once more upon an additional CV in Figure 4, parts J and K. In all these measurements, the feedback current at potentials below 1.2 V, where solely [Fe(CN)₆]^{3-/4-} is observed, changed as a function of the formation of this film. While in Figure 4, parts D and G, the tip current remained near theoretical positive feedback upon returning to low overpotentials, the expansion to higher potential regimes facilitated the creation of a passivating layer, eventually reducing the feedback response, Figure 4J. The opening window CVs therefore cause a change to the surface of the MLG through direct modification of the MLG layers and formation of a new surface layer. To parse out contributions from changes in the MLG interface on sample reactivity, we further performed experiments under modified oxidation conditions to determine the relative contribution of these

When a potential step to 2.5 V versus Ag/AgCl was applied chronoamperometrically to a fresh sample of MLG, the currents at both tip and substrate decreased with time (Figure 5A). As time progressed during the applied positive potential, the tip current shifted from positive feedback to negative feedback (Figure 5B). This decrease in feedback corresponded to a change in the rate constant for electron transfer by over 2 orders of magnitude. The chronoamperometric step at 2.5 V triggered several structural changes on the MLG which yielded competing effects on the SECM response. The G peak slightly decreased in intensity during sample oxidation, most notably in the first 20 s, likely from some exfoliation of the MLG (inset Figure 5C). Following this exfoliation, an abrupt change in L_D was observed (Figure 5C), as the D peak intensity grew rapidly to 250% of the original peak intensity. The increase in the D peak intensity likely arises from the induction of carbon oxides

(e.g., quinones, carboxylates) as defects in the MLG. The presence of new redox-active surface species is supported by CVs taken after the in situ experiment (Figure S3). Following the formation of these defects, a large increase in the $C \equiv N$ peak intensity was observed, although the $C \equiv N$ peak was present from the beginning of the data acquisition.

As discussed in Figure 3, a decrease in the number of graphene layers, from \sim 10 to \sim 3, can cause a drop to approximately one-fourth of the original rate constant for electron transfer. On the other hand, an increasing density of defects is expected to increase the electron-transfer rates. Nonetheless, the abrupt decrease in electron-transfer rates observed in Figure 5B is not consistent with either of these effects. There is only a modest recovery of the electron-transfer rates ca. 40 s, when the increase in D peak intensity plateaus. Thus, it seems that the growth of a passivating film derived from $[Fe(CN)_6]^{3-/4-}$ decomposition overwhelms these effects. We speculate that the formation of this passivating film is facilitated by the increase in exfoliation and formation of surface oxides. Approach curves to the surface after completion of the experiment show a greatly passivated surface (Figure S4).

These observations are not in contradiction with previously reported effects of oxygenated defects. 20,24,61 Indeed, measurements on the reactivity of graphene subject to mildly oxidizing conditions via limited CV excursions showed that, as the D peak intensity increased with each set of CVs, so did the k° . An increased reactivity with increased defect density was deduced from the negative correlation of k° with $L_{\rm D}$ (Figure S5). This indicates that activating the MLG in the presence of $[Fe(CN)_6]^{3-}$ in milder conditions does not cause the formation of a blocking layer. In all these experiments, some evidence of C≡N adsorbed on the MLG surface was observed. This implies that the formation of small amounts of the adsorbed layer did not overwhelm the effects of the defects under these mildly oxidizing conditions. The process of controlling the interfacial reactivity of MLG is therefore highly dependent on conditioning methodology. Through the experiments detailed here, we have elucidated four different possible ways to control reactivity, as summarized in Figure 6.

CONCLUSION

Coupled Raman—SECM was introduced as a tool for generating images and data sets of time-dependent in situ spectroscopic features matched to redox reactivity over the same area. We showed that the number of graphene layers

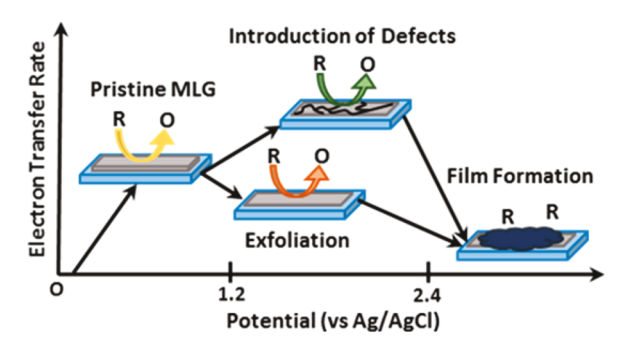


Figure 6. Effect of oxidative potential applied to MLG. As the potential is increased to 1.2 V the kinetics of electron transfer is controlled by the overpotential. Potentials above 1.2 V cause sample exfoliation, decreasing sample reactivity. In this potential window defects are introduced, and mediator adsorption will occur. Above 2.4 V, absorbed mediator decomposes, passivating the interface.

modulates the electron-transfer kinetics, finding a decrease in layers decreases the reactivity by a factor of 4 when transitioning from ~10 to ~3 layers of graphene. Imaging MLG displayed the ability of Raman-SECM to enable sitespecific quantification of kinetics and structure. We further explored the effects of high positive potential regimes on MLG using the Raman-SECM setup. Monitoring the oxidation of MLG allowed us to follow the correlations between changes in surface reactivity and surface modification in real time. We found that applying a large positive potential via chronoamperometric and cyclic voltammetry conditions decreased surface reactivity due to the formation of a passivating layer that contained the C\equiv N moiety as a result of decomposition of the redox mediator. However, changes in reactivity were the result of several competing effects created by the formation of exfoliated, oxidized, and surface-modified graphene. We distinguished these effects by their Raman signatures and the versatility afforded by the SECM. Raman-SECM creates new opportunities to assess the redox reactivity of electrochemical interfaces in real time, providing a powerful approach for studying the materials for energy storage and conversion purposes. Future Raman-SECM experiments developed in our laboratory will display an expanded portfolio of materials analyzed, with an increase in the spatial and time resolution by utilizing smaller probes and spectroscopic enhancement techniques.

ASSOCIATED CONTENT

S Supporting Information

The Supporting Information is available free of charge on the ACS Publications website at DOI: 10.1021/acs.analchem.8b00730.

Sample $L_{\rm D}$ calculation, transmittance of MLG, SEM images of pristine and film-covered MLG, approach curves to MLG before and after an oxidative potential step, Raman spectra and k° vs $L_{\rm D}$ plot of MLG oxidized through mild CV conditioning, and graphene growth and patterning procedures (PDF)

AUTHOR INFORMATION

Corresponding Author

*E-mail: joaquinr@illinois.edu. Phone: +1 217-300-7354.

ORCID ®

Noah B. Schorr: 0000-0002-1582-8594

Joaquín Rodríguez-López: 0000-0003-4346-4668

Author Contributions

The manuscript was written through contributions of all authors.

Notes

The authors declare no competing financial interest.

ACKNOWLEDGMENTS

This work was supported by the National Science Foundation under CHE 17-09391. Sample fabrication and characterization were carried out in part in the Frederick Seitz Materials Research Laboratory Central Research Facilities and Nanotechnology Laboratory, University of Illinois. We acknowledge support from the 2015 SACP Starter Grant for the construction of the Raman—SECM setup used in this work. J.R.-L. acknowledges support from a Sloan Research Fellowship.

REFERENCES

- (1) May, B. M.; Yu, Y.-S.; Holt, M. V.; Strobridge, F. C.; Boesenberg, U.; Grey, C. P.; Cabana, J. *Nano Lett.* **2017**, *17* (12), 7364–7371.
- (2) Figueiredo, M. C.; Trieu, V.; Eiden, S.; Koper, M. T. M. *J. Am. Chem. Soc.* **2017**, 139 (41), 14693–14698.
- (3) Yu, S.-H.; Huang, X.; Schwarz, K.; Huang, R.; Arias, T. A.; Brock, J. D.; Abruña, H. D. *Energy Environ. Sci.* **2018**, *11*, 202–210.
- (4) Dokko, K.; Shi, Q.; Stefan, I. C.; Scherson, D. A. J. Phys. Chem. B **2003**, 107 (46), 12549–12554.
- (5) Lee, C.; Wei, X.; Kysar, J. W.; Hone, J. Science **2008**, 321 (5887), 385–388.
- (6) Bunch, J. S.; Verbridge, S. S.; Alden, J. S.; van der Zande, A. M.; Parpia, J. M.; Craighead, H. G.; McEuen, P. L. *Nano Lett.* **2008**, *8* (8), 2458–2462.
- (7) Ritzert, N. L.; Li, W.; Tan, C.; Rodríguez-Calero, G. G.; Rodríguez-López, J.; Hernández-Burgos, K.; Conte, S.; Parks, J. J.; Ralph, D. C.; Abruña, H. D. *Faraday Discuss.* **2014**, *172*, 27–45.
- (8) Hui, J.; Burgess, M.; Zhang, J.; Rodríguez-López, J. ACS Nano **2016**, 10 (4), 4248–4257.
- (9) Yang, T.; Lin, H.; Zheng, X.; Loh, K. P.; Jia, B. J. Mater. Chem. A 2017, 5 (32), 16537–16558.
- (10) Ambrosi, A.; Chua, C. K.; Bonanni, A.; Pumera, M. Chem. Rev. **2014**, 114 (14), 7150–7188.
- (11) Pimenta, M. A.; Dresselhaus, G.; Dresselhaus, M. S.; Cançado, L. G.; Jorio, A.; Saito, R. *Phys. Chem. Chem. Phys.* **2007**, 9 (11), 1276–1200
- (12) Ferrari, A. C.; Meyer, J. C.; Scardaci, V.; Casiraghi, C.; Lazzeri, M.; Mauri, F.; Piscanec, S.; Jiang, D.; Novoselov, K. S.; Roth, S.; Geim, A. K. Phys. Rev. Lett. **2006**, 97 (18), 187401.
- (13) Malard, L. M.; Pimenta, M. A.; Dresselhaus, G.; Dresselhaus, M. S. *Phys. Rep.* **2009**, 473 (5), 51–87.
- (14) Cançado, L. G.; Jorio, A.; Ferreira, E. H. M.; Stavale, F.; Achete, C. A.; Capaz, R. B.; Moutinho, M. V. O.; Lombardo, A.; Kulmala, T. S.; Ferrari, A. C. *Nano Lett.* **2011**, *11* (8), 3190–3196.
- (15) Barton, Z. J.; Hui, J.; Schorr, N. B.; Rodríguez-López, J. *Electrochim. Acta* **2017**, 241 (Suppl. C), 98–105.
- (16) Joya, K. S.; Sala, X. Phys. Chem. Chem. Phys. 2015, 17 (33), 21094–21103.
- (17) McCreery, R. L. Magnitude of Raman Scattering. In *Raman Spectroscopy for Chemical Analysis*; Winefordner, J. F., Ed.; Chemical Analysis, Vol. 157; John Wiley & Sons, Inc.: New York, 2000; pp 15–33
- (18) Ritzert, N. L.; Rodríguez-López, J.; Tan, C.; Abruña, H. D. Langmuir 2013, 29 (5), 1683–1694.
- (19) Bard, A. J., Mirkin, M. V., Eds. Scanning Electrochemical Microscopy, 2nd ed.; CRC Press: Boca Raton, FL, 2012.
- (20) Tan, C.; Rodríguez-López, J.; Parks, J. J.; Ritzert, N. L.; Ralph, D. C.; Abruña, H. D. ACS Nano **2012**, 6 (4), 3070–3079.

(21) Edwards, M. A.; Bertoncello, P.; Unwin, P. R. J. Phys. Chem. C **2009**, 113 (21), 9218–9223.

- (22) Xie, X.; Zhao, K.; Xu, X.; Zhao, W.; Liu, S.; Zhu, Z.; Li, M.; Shi, Z.; Shao, Y. J. Phys. Chem. C 2010, 114 (33), 14243-14250.
- (23) Nioradze, N.; Chen, R.; Kurapati, N.; Khvataeva-Domanov, A.; Mabic, S.; Amemiya, S. Anal. Chem. **2015**, 87 (9), 4836–4843.
- (24) Zhong, J.-H.; Zhang, J.; Jin, X.; Liu, J.-Y.; Li, Q.; Li, M.-H.; Cai, W.; Wu, D.-Y.; Zhan, D.; Ren, B. J. Am. Chem. Soc. **2014**, 136 (47), 16609–16617.
- (25) Güell, A. G.; Ebejer, N.; Snowden, M. E.; Macpherson, J. V.; Unwin, P. R. J. Am. Chem. Soc. **2012**, 134 (17), 7258–7261.
- (26) Ritzert, N. L.; Li, W.; Tan, C.; Rodríguez-Calero, G. G.; Rodríguez-López, J.; Hernández-Burgos, K.; Conte, S.; Parks, J. J.; Ralph, D. C.; Abruña, H. D. Faraday Discuss. 2014, 172, 27–45.
- (27) McCreery, R. L.; McDermott, M. T. Anal. Chem. 2012, 84 (5), 2602–2605.
- (28) Zhang, G.; Tan, S.-Y.; Patel, A. N.; Unwin, P. R. Phys. Chem. Chem. Phys. **2016**, 18 (47), 32387–32395.
- (29) Amemiya, S. Anal. Chem. 2017, 89 (13), 7269-7272.
- (30) Tan, S.; Zhang, J.; Bond, A. M.; Macpherson, J. V.; Unwin, P. R. Anal. Chem. **2016**, 88 (6), 3272–3280.
- (31) Etienne, M.; Dossot, M.; Grausem, J.; Herzog, G. Anal. Chem. **2014**, 86 (22), 11203–11210.
- (32) Gossage, Z. T.; Schorr, N. B.; Hernández-Burgos, K.; Hui, J.; Simpson, B. H.; Montoto, E. C.; Rodríguez-López, J. *Langmuir* **2017**, 33 (37), 9455–9463.
- (33) Steimecke, M.; Seiffarth, G.; Bron, M. Anal. Chem. 2017, 89 (20), 10679–10686.
- (34) An, S. J.; Li, J.; Daniel, C.; Mohanty, D.; Nagpure, S.; Wood, D. L. Carbon **2016**, *105* (Suppl. C), 52–76.
- (35) Chattopadhyay, S.; Lipson, A. L.; Karmel, H. J.; Emery, J. D.; Fister, T. T.; Fenter, P. A.; Hersam, M. C.; Bedzyk, M. J. *Chem. Mater.* **2012**, 24 (15), 3038–3043.
- (36) Collins, J.; Gourdin, G.; Foster, M.; Qu, D. Carbon 2015, 92 (Suppl. C), 193-244.
- (37) Adams, B. D.; Black, R.; Radtke, C.; Williams, Z.; Mehdi, B. L.; Browning, N. D.; Nazar, L. F. ACS Nano **2014**, 8 (12), 12483–12493.
- (38) Carino, E. V.; Newman, D. J.; Connell, J. G.; Kim, C.; Brushett, F. R. *Langmuir* **2017**, 33 (43), 11911–11918.
- (39) Burgess, M.; Hernández-Burgos, K.; Simpson, B. H.; Lichtenstein, T.; Avetian, S.; Nagarjuna, G.; Cheng, K. J.; Moore, J. S.; Rodríguez-López, J. *J. Electrochem. Soc.* **2016**, *163* (4), H3006–H3013.
- (40) Kundu, D.; Black, R.; Adams, B.; Nazar, L. F. ACS Cent. Sci. **2015**, 1 (9), 510-515.
- (41) Chen, Y.; Freunberger, S. A.; Peng, Z.; Fontaine, O.; Bruce, P. G. Nat. Chem. **2013**, 5 (6), 489–494.
- (42) Ventosa, E.; Schuhmann, W. Phys. Chem. Chem. Phys. 2015, 17 (43), 28441–28450.
- (43) Zampardi, G.; Klink, S.; Kuznetsov, V.; Erichsen, T.; Maljusch, A.; La Mantia, F.; Schuhmann, W.; Ventosa, E. *ChemElectroChem* **2015**, 2 (10), 1607–1611.
- (44) Bülter, H.; Peters, F.; Schwenzel, J.; Wittstock, G. Angew. Chem., Int. Ed. 2014, 53 (39), 10531–10535.
- (45) Ferrari, A. C. Solid State Commun. 2007, 143 (1), 47-57.
- (46) Graf, D.; Molitor, F.; Ensslin, K.; Stampfer, C.; Jungen, A.; Hierold, C.; Wirtz, L. *Nano Lett.* **2007**, *7* (2), 238–242.
- (47) Wang, Y. y.; Ni, Z. h.; Yu, T.; Shen, Z. X.; Wang, H. m.; Wu, Y. h.; Chen, W.; Shen Wee, A. T. *J. Phys. Chem. C* **2008**, *112* (29), 10637–10640.
- (48) Nair, R. R.; Blake, P.; Grigorenko, A. N.; Novoselov, K. S.; Booth, T. J.; Stauber, T.; Peres, N. M. R.; Geim, A. K. Science 2008, 320 (5881), 1308–1308.
- (49) Lefrou, C.; Cornut, R. ChemPhysChem 2010, 11 (3), 547-556.
- (50) Zhu, W.; Perebeinos, V.; Freitag, M.; Avouris, P. Phys. Rev. B: Condens. Matter Mater. Phys. 2009, 80 (23), 235402.
- (51) Holzwarth, J.; Amsharov, K. Y.; Sharapa, D. I.; Reger, D.; Roshchyna, K.; Lungerich, D.; Jux, N.; Hauke, F.; Clark, T.; Hirsch, A. *Angew. Chem., Int. Ed.* **2017**, *56* (40), 12184–12190.

(52) Ohta, T.; Bostwick, A.; McChesney, J. L.; Seyller, T.; Horn, K.; Rotenberg, E. *Phys. Rev. Lett.* **2007**, *98* (20), 206802.

- (53) Brownson, D. A. C.; Varey, S. A.; Hussain, F.; Haigh, S. J.; Banks, C. E. *Nanoscale* **2014**, *6* (3), 1607–1621.
- (54) Hathcock, K. W.; Brumfield, J. C.; Goss, C. A.; Irene, E. A.; Murray, R. W. Anal. Chem. 1995, 67 (13), 2201–2206.
- (55) Alliata, D.; Kötz, R.; Haas, O.; Siegenthaler, H. Langmuir 1999, 15 (24), 8483–8489.
- (56) Alsmeyer, D. C.; McCreery, R. L. Anal. Chem. 1992, 64 (14), 1528-1533.
- (57) Kneten, K. R.; McCreery, R. L. Anal. Chem. 1992, 64 (21), 2518–2524.
- (58) Hui, J.; Zhou, X.; Bhargava, R.; Chinderle, A.; Zhang, J.; Rodríguez-López, J. *Electrochim. Acta* 2016, 211 (Suppl. C), 1016–1023
- (59) Beriet, C.; Pletcher, D. J. Electroanal. Chem. 1993, 361 (1), 93-101.
- (60) Loo, B. H.; Lee, Y. G.; Liang, E. J.; Kiefer, W. Chem. Phys. Lett. 1998, 297, 83–89.
- (61) Su, C.; Loh, K. P. Acc. Chem. Res. 2013, 46 (10), 2275-2285.
- (62) Fleischmann, M.; Graves, P. R.; Robinson, J. J. Electroanal. Chem. Interfacial Electrochem. 1985, 182 (1), 87–98.